Ionics (2020) 26:6233–6244
https://doi.org/10.1007/s11581-020-03752-w

ORIGINAL PAPER

Structural, thermal and electrical study of copper-doped strontium zirconate

Paramvir Kaur[1] · K. Singh[1]

Received: 22 June 2019 / Revised: 5 July 2020 / Accepted: 23 August 2020 / Published online: 5 September 2020

Abstract

Copper-doped $SrZrO_3$ perovskites prepared via solid-state reaction method are studied for structural, morphological, thermal and electrical properties using various characterisation techniques. The X-ray diffraction and Rietveld refinement confirm the monophasic orthorhombic structure of the undoped and doped samples. The shifting of the XRD peaks with doping is the manifestation of dopant Cu into the Zr site of $SrZrO_3$ lattice. The thermal expansion curves of doped and undoped samples vary linearly with temperature. The conductivity of the samples increases with copper doping. The activation energy of the samples suggests mixed electronic and ionic (protonic) conduction in the present samples. The conductivity of the doped $SrZrO_3$ increases up to three orders, i.e. 10^{-4} S cm^{-1} at 600 °C. The thermal and electrical properties are in the required SOFC range making Cu-doped $SrZrO_3$ suitable for use as cathode materials.

Keywords Copper-doped strontium zirconate · Oxygen vacancy · Impedance spectroscopy · Dilatometry · Solid oxide fuel cell

Introduction

Over the past few years, a lot of research is going on the development of materials for intermediate-temperature solid oxide fuel cells (IT-SOFCs) [1–3]. One of the members of the $A^{2+}B^{4+}O_3$-structured perovskite oxide family is $SrZrO_3$. Owing to its high melting point (~2600 °C), chemical stability and fast ionic (protonic) conduction at high temperatures, $SrZrO_3$ finds applications as cathode and electrolyte materials in IT-SOFCs [4–6]. Numerous researchers have been studying the evolution of different structural phase transitions of $SrZrO_3$ [7, 8]. Basically, with the rise in the temperature, there is a decrement in the tilt angle of the ZrO_6 octahedra which is responsible for the different phase transitions in $SrZrO_3$. As the literature suggests, $SrZrO_3$ has orthorhombic (*Pbnm*) structure at room temperature [9]. However, with the rise in temperature, $SrZrO_3$ undergoes three phase transformations namely, orthorhombic (*Pbnm*) → orthorhombic (*Cmcm*) → tetragonal (*I4/mcm*) → cubic (*Pm3m*) at room temperature (RT), 700, 830 and 1170 °C, respectively [10].

These structural phase transitions have been studied using various techniques such as high-temperature X-ray diffraction and neutron powder diffraction [7, 8]. Thermal analytical techniques such as differential scanning calorimetry (DSC), differential thermal analysis (DTA) and dilatometry have also been used to study these high-temperature phase transitions [10–13]. Apart from the structural phase transitions, thermal expansion is also an important parameter. Zhao et al. observed how the phase transitions affect the bond lengths of the octahedra of the zirconates, which further influences their thermal expansion [14]. Raman spectroscopy is also used since the variation in the chemical bonds of the materials plays an essential role in the phase transitions [15]. The role of doping rare earth elements such as Sm^{3+}, Pb^{2+}, Eu^{3+} and Tb^{3+} and transition metals such as Ni^{2+} and $Fe^{3+/4+}$ in the $SrZrO_3$ system has been of keen interest due to the easy tuning of the optical properties of these perovskites [16–19].

Perovskite-structured materials which have transition elements at the B-site show metallic, superconducting or mixed conducting behaviour due to their multiple valence states [20]. Depending upon the size, charge and the concentration of the dopant, the addition of transition metals at the B-site of the perovskite-structured materials enhances their ionic as well as electronic properties [21]. Misra et al. studied the electrical conducting behaviour of Fe-doped $SrZrO_3$. Doping of 10 mol% Fe enhanced the conductivity but further increased

✉ K. Singh
kusingh@thapar.edu

[1] School of Physics and Materials Science, Thapar Institute of Engineering and Technology, Patiala, Punjab 147004, India

leads to the formation of a secondary phase [22]. Tang et al. studied its structural and magnetic properties where Fe enhanced the dielectric properties and also induced ferromagnetism in $SrZrO_3$ [23].

The charge difference between the host (B-site cation) and the lower valence dopant leads to the creation of oxide ion vacancies in the $SrZrO_3$ system. The vacancy formation affects the BO_6 octahedra, which alters the thermal and electrical properties of the system. The role of oxygen vacancies is prominent since it provides vacant sites for ionic (protonic) conduction. The oxide ion conductors turn out to be protonic in hydrogen-containing atmospheres. Water from the gas-phase dissociates into hydroxide ion and a proton. The hydroxide ion fills the oxide ion vacancy while the proton forms a covalent bond with the lattice oxygen [24, 25]. The thermal properties of the system are affected by the ordering and disordering of the vacancies. Also, the change in the valence state of the B-site cation and the creation of oxygen vacancies maintain the neutrality of the system [26, 27]. Existence of multiple valence state elements at the B-site enables the movement of electrons in the crystal lattice. So, a significant role is played by the B-site cations in controlling the conducting behaviour of these oxides.

However, there are no reports regarding the structural, thermal and electrical properties of doping CuO at the B-site of $SrZrO_3$. These properties are essential for the materials to be tested as cathode and electrolyte for IT-SOFCs. The present study is, therefore, focused on the structure-supported thermal and electrical conductivity of $SrZr_{1-x}Cu_xO_3$ ($0 \le x \le 0.20$). X-ray diffraction (XRD), X-ray photoelectron spectroscopy (XPS), Fourier-transform infrared spectroscopy (FTIR) and scanning electron microscopy with attached energy dispersive spectroscopy (SEM-EDS) have been used to gain knowledge about the structure and morphology of the samples. The thermal and electrical properties have been studied using thermogravimetric (TG) and differential thermal analyser (DTA), dilatometry and impedance spectroscopy.

Materials and methods

Five compositions of the $SrZr_{1-x}Cu_xO_3$ ($0 \le x \le 0.20$) system were synthesised using the solid-state reaction route. These chemicals are used as received from the suppliers without any further purification. Stoichiometric ratios of $SrCO_3$, ZrO_2 and CuO powders were mixed thoroughly in acetone media for 2 h using agate mortar and pestle. The powders were calcined at 800 °C for 10 h and then pelletised using a hydraulic press. The green pellets of the doped samples were sintered at 1200 °C for 5 h in the air by heating them in a high-resistance furnace. The samples were furnace cooled to room temperature. The undoped sample used for comparison study was sintered at 1500 °C for 5 h in the air. Crystalline structures of the prepared powders were identified via XRD (PANalytical X'Pert Pro) using Ni-filtered Cu-K_α radiation (λ = 1.5406 Å). The measurements were carried out in the angular range of 20–80° with a step size of 0.017°. The XRD patterns are refined by Rietveld refinement using FullProf Software. The oxidation state of Cu has been confirmed through XPS (PHI-5000 VersaProbe III, Physical Electronics) using Al-K_α radiation (1486.6 eV) with carbon peak as the reference.

Infrared spectra of the samples were observed at room temperature using FTIR spectroscopy (Spectrum RX-I, Perkin Elmer) in the spectral range of 1800–400 cm^{-1}. The powders of the crushed, sintered pellets were mixed with potassium bromide and pressed to form translucent pellets for use in the FTIR spectra measurements. The surface morphology of the samples was examined using SEM (JSM-6510 LV, JEOL). A thin layer of gold is sputtered onto the surface of the sintered pellets with the help of an Auto fine coater (JEC-1600, JEOL) to make them conducting. The grain size calculations were done using Zeiss Axiovision software. EDS analysis was carried out using an INCA attachment coupled with SEM to check the difference in the stoichiometry of the undoped and doped samples.

The TG-DTA (Diamond Pyris, Perkin Elmer) measurements were carried out by placing the powders of the sintered pellets in an alumina pan and heating them at a rate of 10 °C min^{-1} in nitrogen. A push-rod-type dilatometer (DIL 402 PC, Netzsch) was used to carry out the thermal expansion measurements of the samples. The coefficient of thermal expansion (CTE) of the sintered samples was measured from 200 to 600 °C at a heating rate of 5 °C min^{-1}. The reference material used during the measurement was Al_2O_3. Impedance measurements were carried out using an impedance analyser (Solartron SI-1260) in the frequency range of 10^2–10^6 Hz with 0.1 V AC biasing. Before placing the sintered pellets in between the two platinum electrodes, a thin layer of platinum was sputtered onto the surface of the samples to make them conducting.

Results and discussion

XRD analysis

Figure 1a illustrates quite intense and well-defined peaks for all the samples depicting the high level of crystallinity or long-range translational ordering. The XRD patterns of all the samples correspond to the orthorhombic phase of $SrZrO_3$ with space group *Pbnm*. The XRD results of $SrZr_{1-x}Cu_xO_3$ ($0 \le x \le 0.20$) have been verified by Rietveld refinement. The samples were refined with both orthorhombic as well as cubic phases; however, the best fit was observed for the orthorhombic phase. The Rietveld refinement of the samples shows good

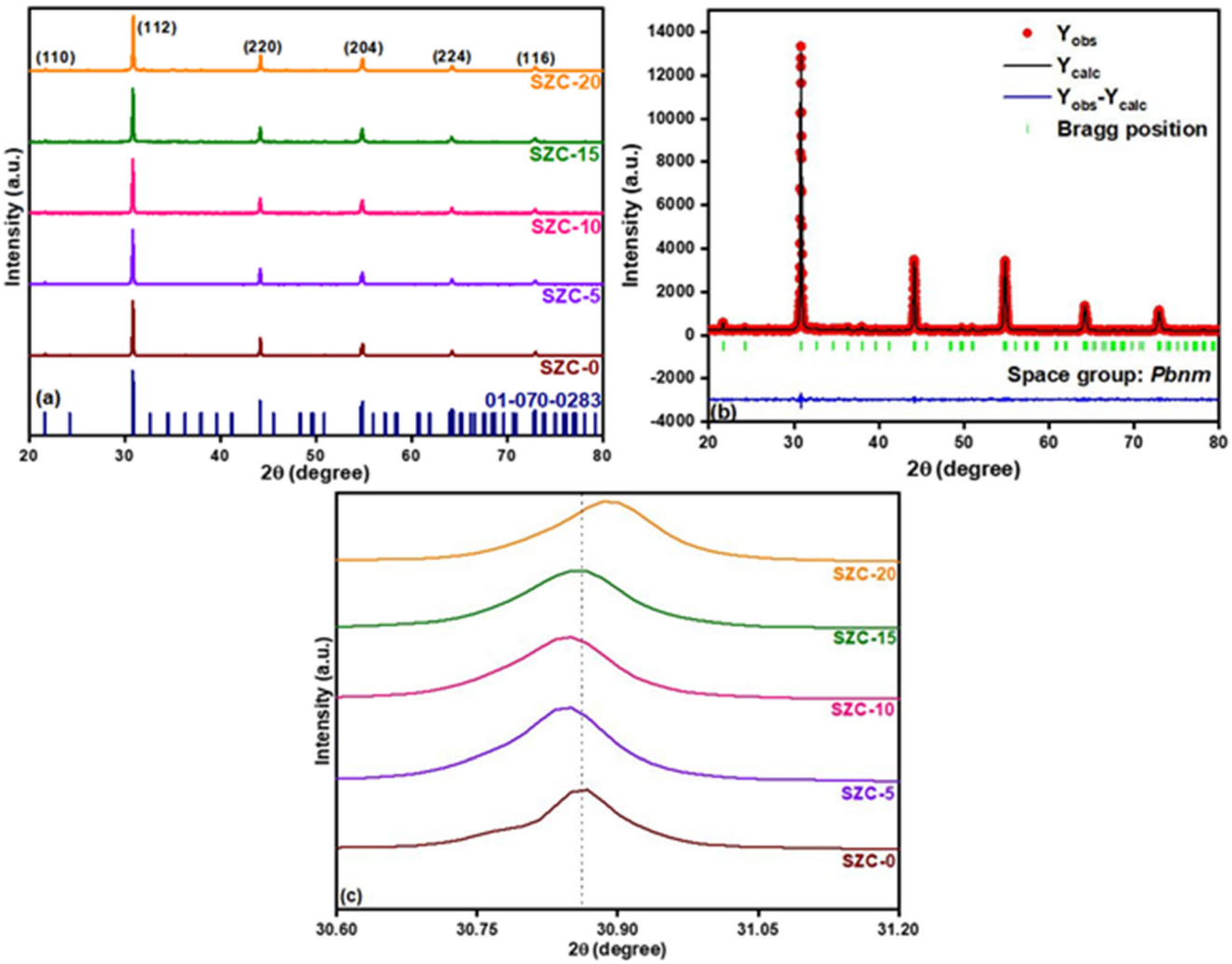

Fig. 1 **a** XRD patterns of $SrZr_{1-x}Cu_xO_3$ ($0 \le x \le 0.20$). **b** Refined XRD pattern of SZC-10 confirming orthorhombic structure with Pbnm space group. **c** Shifting of the highest intense peak (112) towards lower angles depicting the incorporation of CuO in the $SrZrO_3$ system

agreement between the observed and calculated pattern since the Chi-square (χ^2) value of all the samples approaches to 1. As a representative, the refined patterns of SZC-10 are shown in Fig. 1b while the lattice parameters of all the samples are listed in Table 1. The variation of the lattice parameters is in accordance with the shifting of the XRD peaks. The sudden decrease in the lattice parameters of SZC-15 indicates the solid solubility limit of the samples is up till SZC-10. A similar observation has been reported by Kant et al. [28]. This decrease might be associated with the gradual change in the oxidation state of copper from Cu^{1+} to Cu^{2+}. The lattice parameters vary linearly with the doping which indicates the formation of a single phase. The phase formation can also be estimated from the Goldschmidt's tolerance factor (t), which is defined as:

$$t = \frac{r_A + r_O}{\left(\frac{r_B + r_{B'}}{2}\right) + r_O} \quad (1)$$

where r_A, r_O, r_B and $r_{B'}$ are ionic radii of Sr, O, Zr and Cu, respectively. Since CuO is substituted at the B-site so instead of using r_B in Eq. (1), $\frac{r_B + r_{B'}}{2}$ is considered. A tolerance factor of 0.71–0.9 confirms the orthorhombic phase formation [29]. On calculating the tolerance factor of the present samples using Eq. (1), it is inferred that the system is indeed

Table 1 Sample labels and lattice parameters of $SrZr_{1-x}Cu_xO_3$ ($0 \le x \le 0.20$)

Composition	Sample label	a (Å)	b (Å)	c (Å)	V (Å^3)	χ^2
$SrZrO_3$	SZC-0	5.785	5.812	8.194	275.54	0.99
$SrZr_{0.95}Cu_{0.05}O_3$	SZC-5	5.788	5.812	8.194	275.75	1.00
$SrZr_{0.90}Cu_{0.10}O_3$	SZC-10	5.792	5.813	8.196	276.03	1.03
$SrZr_{0.85}Cu_{0.15}O_3$	SZC-15	5.789	5.812	8.194	275.76	1.03
$SrZr_{0.80}Cu_{0.20}O_3$	SZC-20	5.792	5.813	8.198	275.07	1.75

Table 2 Coordination No. (CN), ionic radii (IR), electro-negativity and field strength (F) of different cations used in this study [30]

Cations	Coordination No.	Ionic radii (Å)	Electro-negativity	Field strength
Sr^{2+}	12	1.44	0.95	0.70
Zr^{4+}	6	0.72	1.33	1.88
Cu^{1+}	6	0.77	1.90	0.46
Cu^{2+}	6	0.73	1.90	0.93

orthorhombic since the value of *t* comes out to be 0.85. It is consistent with the XRD results. Table 2 lists the ionic radii (IR) of the elements used in the present composition along with their corresponding coordination numbers (CN) [30]. It is expected that Cu ions will occupy the Zr site due to their minimum ionic radii difference as compared with Sr site. Since the ionic radii of the host, Zr^{4+} (CN = 6, IR = 0.72 Å) is slightly lesser than the dopant, Cu^{2+} (CN = 6, IR = 0.73 Å), therefore, the incorporation of Cu into the host lattice does not change the crystal structure of $SrZrO_3$. However, the local structure of $SrZrO_3$ gets modified due to the charge difference between $Cu^{1+/2+}$ and Zr^{4+}. These modifications are related to the bending of the Zr–O octahedra [31].

It is a well-known fact that doping causes shifting of the XRD peaks along with variation in the intensity. Shifting of the XRD peaks of the doped samples towards lower diffraction angles as seen in Fig. 1c is due to the introduction of larger ionic radii dopant $Cu^{1+/2+}$ (CN = 6, IR = 0.77/0.73 Å) in place of Zr^{4+} (CN = 6, IR = 0.72 Å). On the other hand, the formation of oxygen vacancies shifts the XRD peaks towards higher diffraction angle since the ionic radii of oxygen vacancy is lower than the oxygen ion [32]. Furthermore, shifting of the SZC-20 towards higher angles could be attributed to the change in the valence state of Cu since the ionic radii of Cu^{2+} (CN = 6, IR = 0.73 Å) is slightly greater than Zr^{4+} (CN = 6, IR = 0.72 Å). There might be a possibility of copper to be in Cu^{1+} state initially (SZC-5 and SZC-10) which gradually changes into Cu^{2+} state, particularly in the case of SZC-15 and SZC-20. The XPS results have also verified this change in the oxidation state of Cu. As seen in Fig. 2, Cu is in the mixed-valence state particularly in SZC-5 and SZC-10; however, in SZC-20, the effect of Cu^{1+} state seems to diminish and Cu^{2+} state is prominent. The presence of a mixed-valence state of copper could also be associated with the broadening of the XPS peaks of SZC-5 and SZC-10. The XPS spectra of SZC-20 sample have defined and sharp peaks which might correspond to the presence of fully oxidised Cu^{2+}. Since the XPS spectra of Cu_2O does not have any satellite peaks, therefore, the oxidation state of Cu is only + 2. Also, from the melting points of CuO (1326 °C) and Cu_2O (1232 °C), it is evident that the CuO phase is more stable [33]. As for the intensity of the XRD peaks, the doped samples are quite intense in comparison with the undoped sample. The intensity of the doped samples decreases with the increase in the CuO concentration. However, the intensity of SZC-20 increases abruptly indicating better crystallinity with some order. The change in the valence of copper along with the charge difference between Zr^{4+} and $Cu^{1+/2+}$ ions introduces vacancies into the system. The vacancies cause a local modification in the parent lattice which tilts the BO_6 (ZrO_6) octahedra. The following defect relation represents the vacancies introduced in the system on doping CuO in place of ZrO_2 in $SrZrO_3$ [34]:

$$\mathrm{CuO} \rightarrow \mathrm{Cu}'_{\mathrm{Zr}} + O_o^X + V_o^{\cdot\cdot} \tag{2}$$

The defect equilibrium is represented by the following equation:

$$\frac{1}{2}\, O_2\,(\mathrm{g}) + V_o^{\cdot\cdot} \leftrightarrow O_o^X + 2\,\mathrm{h}^{\cdot} \tag{3}$$

These equations are as per the Kröger-Vink notation where Cu'_{Zr} denotes the vacant Zr site, O_o^X represents the oxygen ion at the lattice and $V_o^{\cdot\cdot}$ represents the vacant oxygen site. These vacancies play an essential role in the conduction mechanism of such perovskites [35].

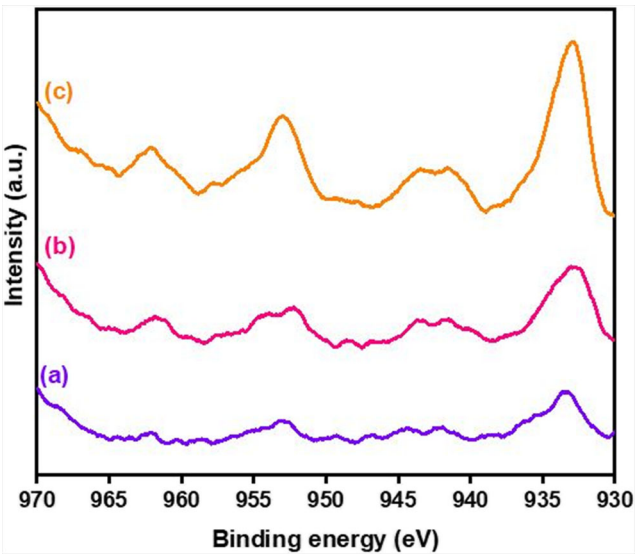

Fig. 2 XPS spectra of Cu in **a** SZC-5, **b** SZC-10 and **c** SZC-20

FTIR analysis

The FTIR spectrum generally exhibits two fundamental modes of vibration, i.e. asymmetric stretching and bending modes which are active under infrared radiation. In a perovskite structure, the bending and stretching vibrations of the B-site cations and oxygen gives rise to the formation of bands of varying intensities [36]. FTIR spectra of $SrZr_{1-x}Cu_xO_3$ ($0 \le x \le 0.20$) as observed from Fig. 3a, b show the existence of seven bands positioned around 1632, 1472, 1210, 1092, 993, 860 and 588 cm^{-1}, respectively. The bands after 1800 cm^{-1} are supposed to be of stretching and bending vibrations of adsorbed water molecules. Therefore, only the fingerprint region (1800–400 cm^{-1}) has been considered for analysing the FTIR spectra of $SrZr_{1-x}Cu_xO_3$ ($0 \le x \le 0.20$). The variation in the position of the bands of the undoped and doped samples is attributed to the presence of oxygen vacancies in the system [37].

The region between 850 and 400 cm^{-1} is attributed to the B–O vibrations, which, in this case, can either be of Zr–O or Cu–O [38]. The bands at 598 and 588 cm^{-1} for the undoped and doped samples correspond to the Zr–O stretching vibrations [39, 40]. In the case of ceramic materials, the shifting of peaks towards higher or lower wavenumbers is related to the formation of stronger and weaker B–O bonds, respectively. The shifting of the bands ~ 598, 1095 and 1233 cm^{-1} towards lower wavenumber might be due to the partial substitution of $Cu^{1+/2+}$ in place of Zr^{4+}. Since the force constant decreases on doping $Cu^{1+/2+}$ into $SrZrO_3$ system, it leads to lower Cu–O strength. It, in turn, causes the bands to shift towards lower wavenumber [41]. Also, the introduction of CuO into the $SrZrO_3$ system induces oxygen vacancies which might also be responsible for the shifting of these bands towards lower wavenumber [42]. The bands at 1461 and 1472 cm^{-1} in the undoped and doped samples, respectively, could be due to the reaction of the samples with CO_2 present in the atmosphere. The water-related bands at ~ 1626 and 1632 cm^{-1} in the undoped sample shift towards higher wavenumber, and the intensity of these bands increases with the increase in the CuO doping thereby confirming higher hydrophilic nature of the doped samples [43–45].

Physical parameters

In order to have a better understanding of the microstructure of the system, it is necessary to have some knowledge about the physical parameters such as density and molar volume. Table 3 lists the different physical parameters used in this study. Density plays a vital role in controlling the properties of polycrystalline materials [45]. The density of the samples was calculated using the concept of Archimedes principle. The following formula has been used for the density calculations:

$$\rho = \frac{W_a}{W_x} \times \rho_x \tag{4}$$

where the density of the sample is ρ, ρ_x is the density of xylene which is 0.863 g cm^{-3}, W_a is the weight of the sample in air and W_x weight of the sample after dipping in xylene. An increase in the CuO concentration leads to a significant increase in the density of the samples. In the present case, copper doping seems to increase the sinterability of the samples as observed in the following section which leads to an increase in the density. The sample with the maximum amount of dopant (SZC-20) is denser than other samples. Since density is an additive property of material, this increase is attributed to the doping of CuO (6.31 g cm^{-3}) which is denser than ZrO_2 (5.68 g cm^{-3}). The molar volume of the samples is also following the expected results. The molar volume (V_m) was calculated using the following formula:

$$V_m = \frac{m}{\rho} \tag{5}$$

where m is the molar mass of $SrZr_{1-x}Cu_xO_3$ ($0 \le x \le 0.20$) and ρ is the density calculated using Eq. (4). Since CuO (79.545 g mol^{-1}) has lesser molar mass than ZrO_2 (123.218 g mol^{-1});

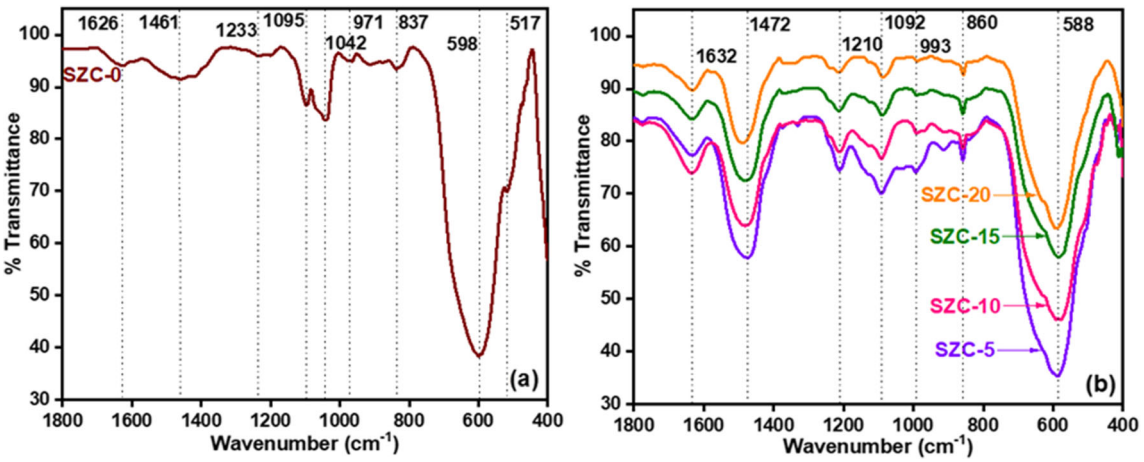

Fig. 3 FTIR spectra of **a** undoped and **b** Cu-doped $SrZrO_3$

Table 3 Relative density, molar volume, concentration, polaron radius and the distance between Cu ions of $SrZr_{1-x}Cu_xO_3$ ($0 \le x \le 0.20$)

Sample label	ρ (%)	V_m ($cm^3\ mol^{-1}$)	N ($\times 10^{22}\ cm^{-3}$)	r_p (cm)	R ($\times 10^{-8}$ cm)
SZC-0	70.73	30.89	–	–	–
SZC-5	85.57	25.19	7.57	9.52×10^{-9}	2.36
SZC-10	90.04	23.66	3.95	1.18×10^{-8}	2.93
SZC-15	92.32	22.78	2.68	1.34×10^{-8}	3.33
SZC-20	93.08	22.30	2.01	1.48×10^{-8}	3.67

therefore, there is a decrease in the values of the molar volume. The highly dense SZC-20 has the lowest molar volume. The density and molar volume of the samples are listed in Table 3. Using the density of the materials, several other parameters such as the concentration of Cu ions per unit volume (N), distance between Cu ions (R) and polaron radius (r_p) are calculated. The ionic concentration is calculated using the following formula:

$$N = \frac{\rho N_a}{100 \times m} \tag{6}$$

where N_a is the Avogadro's number and m is the molecular weight of CuO in the sample. The concentration of ions per unit volume helps to calculate the values of the distance between Cu ions and the polaron radius. These parameters are calculated using the following formulas [46]:

$$R = \sqrt[3]{\frac{1}{N}} \tag{7}$$

$$r_p = 0.5 \times \sqrt[3]{\frac{\pi}{6N}} \tag{8}$$

The decrease in the value of N leads to an increase in the distance between the Cu ions. Therefore, SZC-5 has the lowest value of R. Since, the polaron radius of all the samples is smaller than R but higher than the ionic radii of Cu, it is inferred that the electrons in the system are localised [46].

Morphological analysis

Figure 4a–e illustrates the micrographs of $SrZr_{1-x}Cu_xO_3$ ($0 \le x \le 0.20$) showing the formation of well-defined grains. Change in the morphology of the samples is quite evident from the SEM micrographs. SZC-0, SZC-5 and SZC-20 samples have homogeneously distributed spherical shaped grains. However, in the case of SZC-10, the grains are intact but not uniform in shape. Rather, there is a transition from spherically shaped grains to cubic shaped. The spherically shaped grains somewhat change into inhomogeneously distributed cubic-shaped grains in SZC-15. The intergranular connectivity confirms the effective doping of copper into the $SrZrO_3$ system which is supported by the decrease in the grain size of the doped samples in comparison with the undoped sample. The grain size decreases significantly in SZC-15 and again increases for SZC-20. The XRD analysis also supports this change in the morphology of the samples. Table 4 lists the average grain size values of $SrZr_{1-x}Cu_xO_3$ ($0 \le x \le 0.20$) calculated using the intercept method [47]. The grain size of the samples varies between 0.4 and 1.0 μm. Due to the decrease in the grain size, there is room to accommodate a greater number of grains.

Addition of CuO has been known to refine the microstructure and increase the density of the samples leading to lower sintering temperatures. The lower melting point of CuO favours the liquid phase sintering, which leads to higher density due to increased diffusion process [48]. The density measurements of the samples also support this argument (Fig. 5). The EDS data of the samples listed in Table 4 confirm that the required stoichiometry is maintained even after sintering at a higher temperature.

Thermogravimetric analysis

Figure 6 shows the TG plots of SZC-0, SZC-10 and SZC-20. All the samples undergo discontinuous weight loss when heated up to 1000 °C, which is correlated to the loss of water or lattice oxygen from the system. The weight loss in the undoped and doped samples occurs at three different stages. The first stage of the weight loss occurs until ~ 400 °C. It is less than 0.5% which might be due to the evaporation of moisture (H_2O) from the closed pores or due to the relaxation processes occurring within the system [49, 50]. Between 500 and 800 °C, all the samples show weight loss; however, it is higher in the doped samples, i.e. SZC-10 and SZC-20. This weight loss might be associated with the lattice oxygen loss due to the change in the oxidation states of the transition element, i.e. Cu in the samples. Above 800 till 1000 °C, the change in the weight becomes constant in all the samples. This means that the system is stable in this range and suitable for use as cathode material for SOFCs. Figure 7 shows the DTA curves of the undoped and doped samples. Above 700 °C, no appreciable peaks are observed. However, lots of disturbance is observed in this temperature range which might be due to the presence of phase transitions as reported in the literature [7, 8, 10].

Table 4 Average grain size and EDS data of $SrZr_{1-x}Cu_xO_3$ ($0 \le x \le 0.20$)

Sample label	Average grain size (μm)	Sr (wt%)	Zr (wt%)	Cu (wt%)	O (wt%)
SZC-0	1.03	36.77	41.84	–	21.39
SZC-5	0.84	37.02	41.48	0.16	21.35
SZC-10	0.80	38.90	39.71	0.29	21.05
SZC-15	0.46	38.88	39.11	0.95	21.06
SZC-20	0.52	38.37	40.31	0.13	21.19

Thermal expansion measurement

Dilatometry is a sensitive experimental tool used to analyse the changes in the length of the material upon heating or cooling. CTE is an essential property for the planar design of IT-SOFCs. The slope of $\frac{dL}{dLo}$ versus temperature plot where *Lo* is the original length of the sample while d*L* is the change in the length gives the value of the CTE. The thermal expansion for a given system is generally a demonstration of two processes. First is due to the formation of oxygen vacancies, and the other one is due to the increased bond strength between the dopant and the host. Thermal expansion for a given system is small for strongly bonded materials in comparison with weakly bonded materials [49].

Figure 8 shows the linear thermal expansion curves of all the samples indicating linear continuous curves of thermal expansion with temperature. All the samples expand linearly with a slight difference in their slopes. Table 5 lists the CTE values of $SrZr_{1-x}Cu_xO_3$ ($0 \le x \le 0.20$) which shows that the doped samples have higher CTE than the undoped sample. It might be due to the presence of oxygen vacancies in the system because of $Cu^{1+/2+}$ doping for Zr^{4+} in $SrZrO_3$. The missing oxygen from the lattice lowers the interatomic bond strength and increases the CTE. The shifting of the bands towards lower wavenumber in the FTIR spectra of the doped samples also supports this decrease in the bond strength [50]. It is supported by the difference in the field strength (F) of the cations also. As seen in Table 2, the field strength of Cu is less in comparison with Zr, which implies that the bond strength

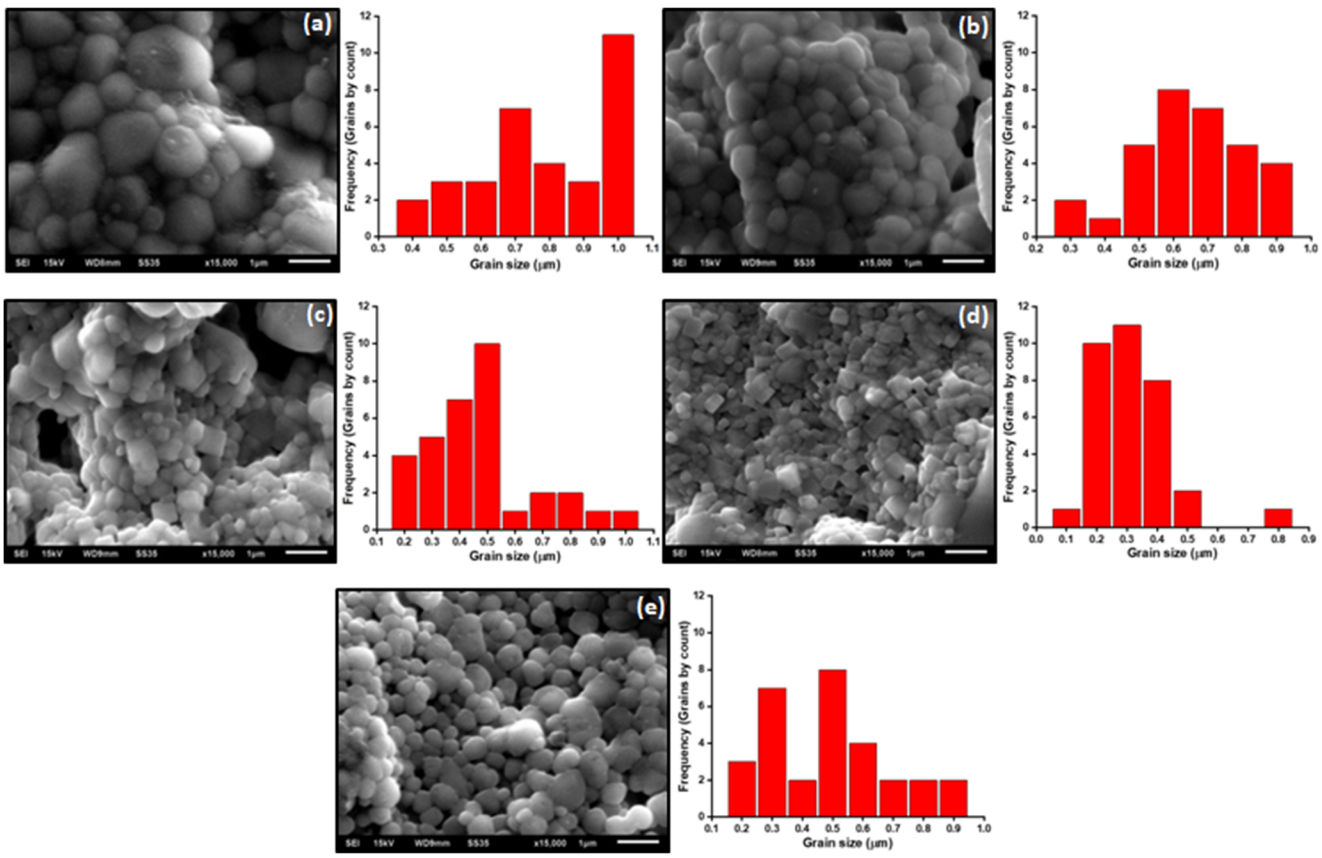

Fig. 4 SEM micrographs of (a) SZC-0, (b) SZC-5, (c) SZC-10, (d) SZC-15 and (e) SZC-20 with corresponding particle size distribution

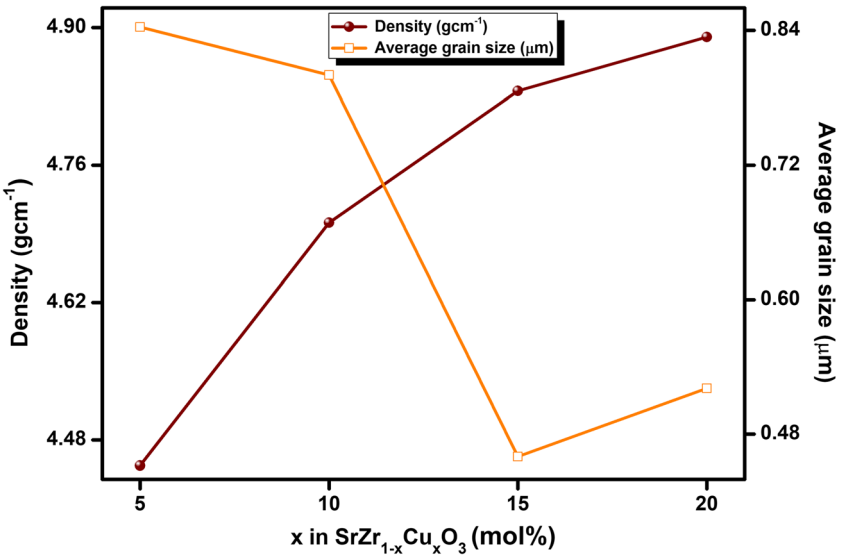

Fig. 5 Variation of density and grain size with an increasing dopant concentration

decreases with Cu substitution. Therefore, the decrease in bond strength increases the CTE of the doped samples in comparison with the undoped samples. The field strength of the cations has been calculated using the following formula:

$$F = \frac{z}{r_c + r_a} \tag{9}$$

where z is the charge of the element, r_c and r_a are the ionic radii of the cation and oxygen (CN = 6, IR = 1.40 Å), respectively.

As the concentration of the dopant increases, a considerable decrease in the CTE values is observed. This decrease is due to the ordering of oxygen vacancies with the CuO concentration. An increase in the vacancies leads to a point where the vacancy concentration becomes ordered. The interaction energy between a cation and anion is a fine balance between the Coulombic attraction and the internuclear repulsion. The ordering of oxygen vacancies makes the potential energy well symmetric, which results in the reduction of the CTE [51, 52]. Also, higher electro-negativity of copper as compared with zirconia leads to an increase in the cation-anion bond (Table 2). It also leads to a decrease in the CTE of the system [53]. However, the CTE values of some of the samples such as SZC-0, SZC-15 and SZC-20 are in the required SOFC range ($9–13 \times 10^{-6}$ °C^{-1}) which make $SrZr_{1-x}Cu_xO_3$ ($0 \le x \le 0.20$) a suitable candidate for use as a cathode for SOFCs.

Electrical properties

The impedance spectroscopy is a well-known non-destructive characterisation technique used to analyse the electrical properties of ceramic materials. It is an essential tool used to relate the microstructures and the contribution of grains to the conductivity of the polycrystalline oxides over a wide range of frequencies and temperatures. The impedance spectroscopy has been extensively utilised to check the suitability of oxide ion conductors for major electrochemical devices such as

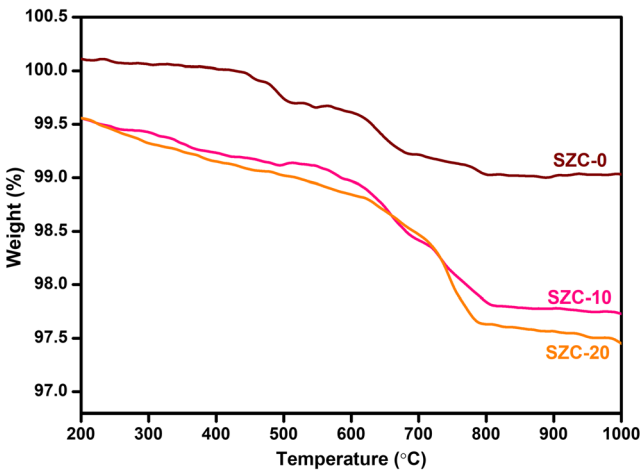

Fig. 6 Representative TG plots of SZC-0, SZC-10 and SZC-20

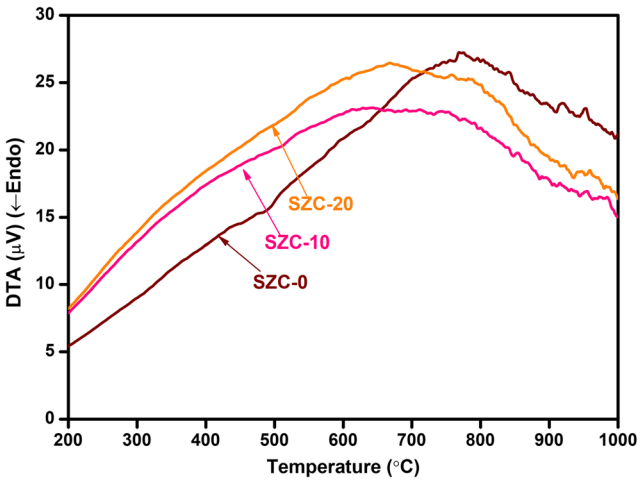

Fig. 7 Representative DTA curves of SZC-0, SZC-10 and SZC-20

Table 5 CTE and total conductivity of $SrZr_{1-x}Cu_xO_3$ ($0 \le x \le 0.20$)

Sample label	CTE ($\times 10^{-6}$ °C^{-1})	σ (S cm^{-1})		
	200–600 °C	200 °C	400 °C	600 °C
SZC-0	12.68	–	5.02×10^{-7}	2.29×10^{-5}
SZC-5	14.37	–	4.35×10^{-6}	8.47×10^{-5}
SZC-10	14.11	9.81×10^{-7}	1.26×10^{-5}	1.06×10^{-4}
SZC-15	11.85	1.72×10^{-5}	7.79×10^{-5}	2.63×10^{-4}
SZC-20	11.57	2.01×10^{-5}	1.50×10^{-4}	1.66×10^{-4}

SOFCs [54, 55]. The conductivity of the $SrZr_{1-x}Cu_xO_3$ ($0 \le x \le 0.20$) is calculated from the Nyquist plots. Generally, a Nyquist plot has three semicircles at different frequencies. The semicircle at the high-frequency region corresponds to the grain while the one at the intermediate frequency region corresponds to the grain boundary. In some cases, a third semicircle is also observed, which corresponds to the electrode contribution [56]. As the temperature increases, the contribution of the grains and grain boundaries keeps on changing, which results in the change of the shape of the semicircles. The point of intersection of the semicircle with the x-axis taken as the resistance. The conductivity (σ) of the samples is then calculated using the following formula:

$$\sigma = \frac{L}{\mathrm{RA}} \tag{10}$$

where L is the thickness and A is the surface area of the platinum sputtered pellets. R is the total resistance, i.e. resistance of the grains as well as grain boundaries of the sample.

Figure 9 shows the representative Nyquist plot of SZC-10 along with the corresponding equivalent circuit. The equivalent circuit consists of series-connected parallel R-C circuit. Due to the presence of depressed semicircles, the constant phase element (CPE) is taken instead of the capacitor. The capacitance of the two semicircles is of the order of 10^{-10} and 10^{-8} F, respectively. Since the capacitance of the second semicircle is two orders higher than the first, it corresponds to the grain boundary while the first corresponds to the grain contribution. Depressed semicircles observed in the samples might be due to varied reasons such as the polycrystalline nature of the samples, surface defects, multiple relaxations, inhomogeneity and dispersion of electrodes [57]. It is observed that the resistance of all the samples decreases considerably with an increase in temperature as well as the dopant concentration. An increase in the temperature gives rise to increased thermal motion of the ions, thereby resulting in higher conductivity. An increase in the CuO concentration enhances the conductivity of the samples due to the electron transfer between the ions of different oxidation states (Fig. 10). Since copper has multiple valence states, it gets randomly distributed in the system. To maintain the overall neutrality of the system, the lower valence dopant also creates oxygen vacancies providing adequate sites for ionic (protonic) conduction. Zr^{4+}, on the other hand, does not contribute much to the conduction phenomena because of the absence of multiple valence states. Therefore, doping of CuO into the system gives rise to the electrical conduction [22]. Table 5 lists the conductivity values of $SrZr_{1-x}Cu_xO_3$ ($0 \le x \le 0.20$). The

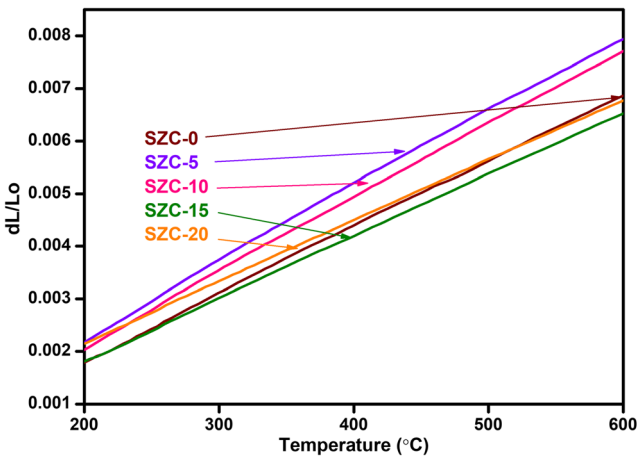

Fig. 8 Thermal expansion curves of $SrZr_{1-x}Cu_xO_3$ ($0 \le x \le 0.20$) measured in the temperature range of 200–600 °C

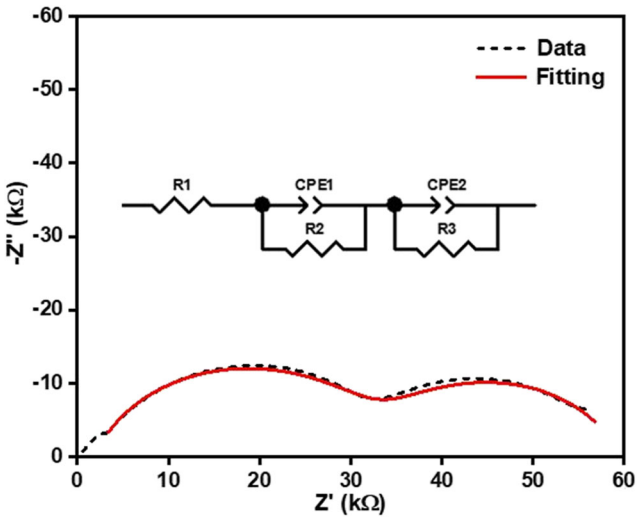

Fig. 9 Representative Nyquist plot of SZC-10 along with equivalent circuit measured at 350 °C

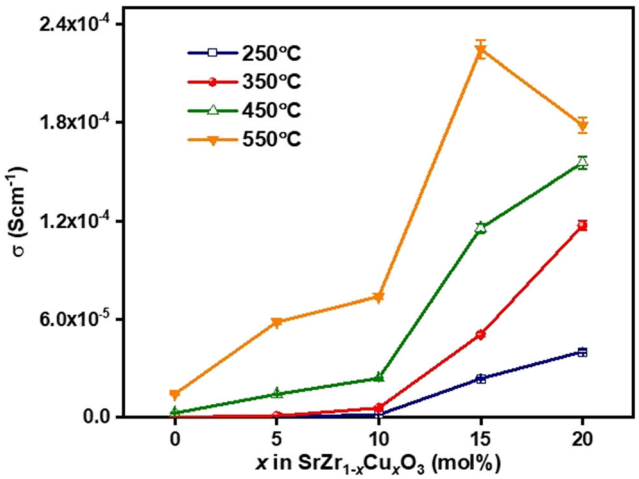

Fig. 10 Variation in the conductivity of $SrZr_{1-x}Cu_xO_3$ ($0 \le x \le 0.20$) with Cu concentration at different temperatures

Table 6 Activation energies of $SrZr_{1-x}Cu_xO_3$ ($0 \le x \le 0.20$)

Samples	Activation energy (eV)	Temperature range (°C)
SZC-0	1.24	350–450
	0.89	450–600
SZC-5	0.93	250–450
	0.71	450–600
SZC-10	0.27	200–300
	0.60	300–600
SZC-15	0.19	200–300
	0.37	300–600
SZC-20	0.33	200–400

conductivities of low dopant concentration, i.e. SZC-0 and SZC-5 are of the order of 10^{-5} S cm^{-1} at 600 °C while of the conductivities of the highly doped samples, i.e. SZC-10, SZC-15 and SZC-20 are of the order of 10^{-4} S cm^{-1} at 600 °C. These conductivity values are higher than that of the Fe-doped $SrZrO_3$, as reported by Misra et al. [22].

As seen in the SEM micrographs, the grain size of the samples decreases with the increase in the CuO concentration. It increases the number of grain boundaries per unit cross-sectional area. Role of grain boundaries become vital in the low-temperature region than in the high-temperature region. It is in accordance with the results that with an increase in the concentration of the dopant, the grain size decreases while the total conductivity increases. Generally, in perovskite materials, oxygen is released at elevated temperatures, thereby increasing the number of randomly distributed oxygen vacancies. Large amounts of oxygen release lead to oxygen vacancy ordering and reduction of the transition metals, which decreases the total conductivity of the system. It results in the decomposition of perovskite oxides into sub-oxides and pure metals [58, 59]. It might be the case with the decreasing conductivity in SZC-20 at 550 °C.

The activation energy of the samples is calculated using the following Arrhenius equation [60, 61]:

$$\sigma T = A \exp\frac{E_a}{kT} \tag{11}$$

where A is a constant, T is the temperature, E_a is the activation energy and k is the Boltzmann constant. The slope of ln σT versus 1000 T^{-1} of the Arrhenius plot gives the activation energy of the system (Fig. 11). The different slopes in the Arrhenius plot attribute to the change in the charge carriers with the rise in temperature. From the decreasing values of E_a given in Table 6, fast mixed electronic and ionic (protonic) conduction with increasing dopant concentration is observed for the samples.

Conclusion

Copper-doped $SrZrO_3$ having orthorhombic structure is synthesised using the solid-state reaction method. Copper doping increases the density of the samples while decreasing the grain size. The charge difference between Cu and Zr leads to the creation of vacancies in the system, which affects the properties of the doped samples. The CTE of all the samples is between 11 and 14 × 10^{-6} $°C^{-1}$ in the temperature range of 200–600 °C which is in the required range for SOFCs. The conductivity of the samples is three orders higher than the undoped sample ~ 10^{-4} S cm^{-1} at 600 °C. The activation energy suggests mixed electronic and ionic (protonic) conduction by the Cu-doped $SrZrO_3$. The thermal expansion and

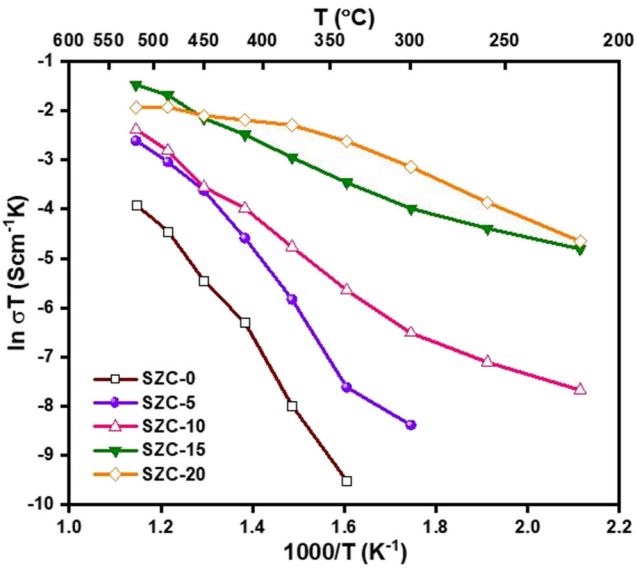

Fig. 11 Arrhenius plot of $SrZr_{1-x}Cu_xO_3$ ($0 \le x \le 0.20$)

electrical conductivity of $SrZr_{1-x}Cu_xO_3$ ($0 \le x \le 0.20$) make it suitable for use as cathode materials in SOFCs.

Acknowledgements The authors would like to acknowledge Sai Labs Thapar Institute of Engineering and Technology, Patiala, SAIF/CIL Panjab University, Chandigarh and IIC Indian Institute of Technology, Roorkee for providing SEM/EDS, XRD and FTIR, XPS and DTA/TGA characterisation facilities, respectively.

Funding This work is financially supported by the Department of Science and Technology (DST), Government of India under the Hydrogen and Fuel Cell (HFC)-2018 project vide letter No. DST/TMD/HFC/2k18/123.

References

1. Mahato N, Banerjee A, Gupta A, Omar S, Balani K (2015) Progress in material selection for solid oxide fuel cell technology: a review. Prog Mater Sci 72:141–337
2. Jun A, Kim J, Shin J, Kim G (2016) Perovskite as a cathode material: a review of its role in solid-oxide fuel cell technology. ChemElectroChem 3:511–530
3. Kaur P, Singh K (2020) Review of perovskite-structure related cathode materials for solid oxide fuel cells. Ceram Int 46:5521–5535
4. Wachsman ED, Kang TL (2011) Lowering the temperature of solid oxide fuel cells. Science 334:935–939
5. Slonimskaya EA, Belyakov AV (2001) Ceramics based on strontium zirconate (a review). Glas Ceram 58(1–2):54–56
6. Shende RV, Krueger DS, Rossetti GA Jr, Lombardo SJ (2001) Strontium zirconate and strontium titanate ceramics for high-voltage applications: synthesis, processing, and dielectric properties. J Am Ceram Soc 84(7):1648–1650
7. Ahtee A, Ahtee M, Glazer AM, Hewat AW (1976) The structure of orthorhombic $SrZrO_3$ by neutron powder diffraction. Acta Cryst B32:3243–3246
8. Kennedy BJ, Howard CJ, Chakoumakos BC (1999) High-temperature phase transitions in $SrZrO_3$. Phys Rev B 59(6):4023–4027
9. Howard CJ, Knight KS, Kennedy BJ, Kisi EH (2000) The structural phase transitions in strontium zirconate revisited. J Phys Condens Matter 12:L677–L683
10. Carlsson L (1967) High-temperature phase transitions in $SrZrO_3$. Acta Cryst 23:901–905
11. Matsuda T, Yamanaka S, Kurosaki K, Kobayashi S (2003) High temperature phase transitions of $SrZrO_3$. J Alloys Compd 351:43–46
12. de Ligny D, Richet P (1996) High-temperature heat capacity and thermal expansion of $SrTiO_3$ and $SrZrO_3$ perovskites. Phys Rev B 53(6):3013–3022
13. Hasegawa S, Sugimoto T, Hashimoto T (2010) Investigation of structural phase transition behaviour of $SrZrO_3$ by thermal analyses and high-temperature X-ray diffraction. Solid State Ionics 181:1091–1097
14. Zhao Y, Weidner DJ (1991) Thermal expansion of $SrZrO_3$ and $BaZrO_3$ perovskites. Phys Chem Miner 18:294–301
15. Fujimori H, Kakihana M, Ioku K, Goto S, Yoshimura M (2004) Structural phase transitions between 700 and 850°C in $SrZrO_3$ studied by Raman spectroscopy. J Ceram Soc Jpn 112(4):189–192
16. Singh N, Seshadri S, Pathak MS, Singh V (2019) Structural and photoluminescence properties of orange perovskites $SrZrO_3$: Sm^{3+} phosphors for solid-state lighting. Solid State Sci 87:163–170
17. Singh N, Kaur S, Jayasimhadri M, Pathak MS, Watanabe S, Gundu Rao TK, Lee J, Singh V (2018) UV emitting Pb^{2+} doped $SrZrO_3$ phosphors prepared by sol-gel procedure. Ceram Int 44(14):17074–17078
18. Das S, Som S, Yang C, Chavhan S, Lu C (2016) Structural evaluations and temperature dependent photoluminescence characterizations of Eu^{3+}-activated $SrZrO_3$ hollow spheres for luminescence thermometry applications. Sci Rep 6: 25787-(1)-(13)
19. Gupta SK, Ghosh PS, Yadav AK, Pathak N, Arya A, Jha SN, Bhattacharyya D, Kadam RM (2016) Luminescence properties of $SrZrO_3/Tb^{3+}$ perovskite: host-dopant energy-transfer dynamics and local structure of Tb^{3+}. Inorg Chem 55:1728–1740
20. Thakur S, Singh K, Pandey OP (2017) Sr doped $BiMO_3$ (M = Mn, Fe, Y) perovskites: Structure correlated thermal and electrical properties. Mater Chem Phys 187:96–103
21. Yajima T, Koide K, Takai H, Fukatsu N, Iwahara H (1995) Application of hydrogen sensor using proton conductive ceramics as a solid electrolyte to aluminium casting industries. Solid State Ionics 79:333–337
22. Misra S (2017) Electrical conductivity and oxygen sensing behaviour of $SrZr_{1-x}Fe_xO_{3-\delta}$ (x = 0 to 0.2). Mater Chem Phys 190:1–7
23. Tang C, Wu Q, Cui Y (2016) Structural, dielectric and magnetic properties of Fe-doped $SrZrO_3$ ceramics. Ceramics-Silikáty 60(2):68–71
24. Yajima T, Suzuki H, Yogo T, Iwahara H (1992) Protonic conduction in $SrZrO_3$-based oxides. Solid State Ionics 51:101–107
25. Davies RA, Islam MS, Gale JD (1999) Dopant and proton incorporation in perovskite-type zirconates. Solid State Ionics 126:323–335
26. Mete E, Shaltaf R, Ellialtioglu S (2003) Electronic and structural properties of a 4d perovskite: Cubic phase of $SrZrO_3$. Phys Rev B 68: 035119-(1)-(4)
27. Richter J, Holtappels P, Graule T, Nakamura T, Gauckler LJ (2009) Materials design for perovskite SOFC cathodes. Montash Chem 140:985–999
28. Kant R, Singh K, Pandey OP (2010) Structural, thermal and transport properties of $Bi_4V_{2-x}Ga_xO_{11-\delta}$ ($0 \le x \le 0.4$). Ionics 16:277–282
29. Goldschmidt VM (1926) Die Gesetze der Krystallochemie. Die Naturwissenschaften 14(21):477–485
30. Shannon RD (1976) Revised effective ionic radii and systematic studies of inert-atomic distances in halides and chalcogenides. Acta Cryst A32:751–767
31. Slodczyk A, Limage M, Colomban P, Zaafrani O, Grasset F, Loricourt J, Sala B (2011) Substitution and proton doping effect on $SrZrO_3$ behaviour: high-pressure Raman study. J Raman Spectrosc 42:2089–2099
32. Omar S, Nino JC (2013) Consistency in the chemical expansion of fluorites: A thermal revision of the doped ceria. Acta Mater 61:5406–5413
33. Kaushik VK (1989) Identification of oxidation states of copper in mixed oxides and chlorides using ESCA. Spectrochim Acta 44B(6):581–587
34. Gellings PJ, Bouwmeester HJM (1997) The CRC handbook of solid state electrochemistry. CRC Press, Boca Raton
35. Thakur S, Devi M, Singh K (2014) Structural and optical properties of La and Gd substituted $Bi_{4-x}M_xV_2O_{11-\delta}$ ($0.1 \le x \le 0.3$). Ionics 20:73–81
36. Gill JK, Pandey OP, Singh K (2012) Ionic conductivity, structural and thermal properties of Ca^{2+} doped $Y_2Ti_2O_7$ pyrochlores for SOFC. Int J Hydrog Energy 37:3857–3864
37. Thakur S, Pandey OP, Singh K (2014) Structural and optical properties of $Bi_{1-x}A_xFeO_3$ (A = Sr, Ca; $0.40 \le x \le 0.55$). J Mol Struct 1074:186–192
38. Prakash V, Diwan RK, Niyogi UK (2015) Characterization of synthesized copper oxide nanopowders and their use in nanofluids for

enhancement of thermal conductivity. Indian J Pure Appl Phys 53: 753–758
39. Zhang L, Wang J, Peng D, Long F, Mo S, Wu Y, Zou Z (2017) Photoluminescence and dielectric properties of pure/Yb-doped $SrZrO_3$ crystals. J Phys Chem Solids 104:1–7
40. Malghe YS, Yadav UC (2015) Synthesis, characterization and investigation of dielectric properties of nanosized $SrZrO_3$. J Therm Anal Calorim 122:589–594
41. Ostos C, Mestres L, Martínez-Sarrión ML, García JE, Albareda A, Perez R (2009) Synthesis and characterization of A-site deficient rare-earth doped $BaZr_xTi_{1-x}O_3$ perovskite-type compounds. Solid State Sci 11:1016–1022
42. Parida S, Rout SK, Subramanian V, Barhai PK, Gupta N, Gupta VR (2012) Structural, microwave dielectric properties and dielectric resonator antenna studies of $Sr(Zr_xTi_{1-x})O_3$ ceramics. J Alloys Compd 528:126–134
43. Chandradas J, Kim KH (2009) Synthesis and characterization of $LaAlO_3$ nanopowders by emulsion combustion method. J Alloys Compd 481:L31–L34
44. Schrader B (Ed.) (1995) Infrared Raman Spectroscopy: Methods and Application, VCN, Weinheim
45. Khirade PP, Shinde AB, Raut AV, Birajdar SD, Jadhav KM (2016) Investigations on the synthesis, structural and microstructural characterizations of $Ba_{1-x}Sr_xZrO_3$ nanoceramics. Ferroelectrics 504(1): 216–229
46. Kashif I, Ratep A (2015) Effect of copper oxide on structure and physical properties of lithium lead borate glasses. Appl Phys A Mater Sci Process 120(4):1427–1434
47. Kaur P, Singh K (2019) Effect of Ni substitution on the structural and optical properties of $SrZr_{1-x}Ni_xO_3$ ($0.05 \le x \le 0.20$) perovskites. J Mol Struct 1180:659–664
48. Guisard Restivo TA, Mello-Castanho SRH (2010) Cu-Ni-YSZ anodes for solid oxide fuel cell by mechanical alloying processing. Int J Mater Res 101:128–132
49. Sood K, Singh K, Pandey OP (2012) Studies on Sr substituted lanthanum indate as mixed ionic conductor. J Mater Sci 47:4520–4529
50. Thakur S, Pandey OP, Singh K (2015) Structural, thermal and electrical study of $BiSr_{0.5}Mn_{0.5}O_3$. Part Sci Technol 33:178–183
51. Shelby JE (2005) Introduction to glass science and technology. Royal Society of Chemistry, Cambridge (2005)
52. Thakur S, Pandey OP, Singh K (2014) Role of Sr^{2+} substitution on the structural, thermal and conducting behaviour of $Bi_{1-x}Sr_xFeO_3$ ($0.40 \le x \le 0.55$). Ceram Int 40:16371–16379
53. Sood K, Singh K, Basu S, Pandey OP (2016) Optical, thermal, electrical and morphological study of $La_{1-x}Ca_xGaO_{3-\delta}$ (x = 0, 0.5, 0.10, 0.15 and 0.20) electrolyte. J Eur Ceram Soc 36(13):3165–3171
54. Borkar H, Barvat A, Pal P, Shukla AK, Pulikkotil JJ, Kumar A (2016) Polaron-electron assisted giant dielectric dispersion in $SrZrO_3$ high-k dielectric. J Appl Phys 119: 214101-(1)-(6)
55. Irvine JTS, Sinclair DC, West AR (1990) Electroceramics: characterization by impedance spectroscopy. Adv Mater 2(3):132–138
56. Yuan X, Song C, Wang H, Zhang J (2010) Electrochemical impedance spectroscopy in PEM fuel cells. Springer, London
57. Tiwari B, Choudhary RNP (2010) Study of impedance parameters of cerium modified lead zirconate titanate ceramics. IEEE Trans Dielectr Electr Insul 17(1):5–17
58. Richter J, Holtappels P, Graule T, Gauckler LJ (2008) Non-stoichiometry, thermal expansion and electrical properties of $Pr_{1-x}Sr_xMn_{1-y}In_yO_{3-\delta}$ perovskites. Solid State Ionics 179:2284–2289
59. Kostogloudis GC, Vasilakos N, Ftikos C (1998) Crystal structure, thermal and electrical properties of $Pr_{1-x}Sr_xCoO_{3-\delta}$ (x = 0,0.15,0.30, 0.4,0.5) perovskite oxides. Solid State Ionics 106:207–218
60. Hussain AM, Pan K, Huang Y, Robinson IA, Gore C, Wachsman ED (2018) Highly performing chromate-based ceramic anodes ($Y_{0.7}Ca_{0.3}Cr_{1-x}Cu_xO_{3-\delta}$) for low-temperature solid oxide fuel cells. ACS Appl Mater Interfaces 10:36075–36081
61. Omar S, Wachsman ED, Nino JC (2006) A co-doping approach towards enhanced ionic conductivity in fluorite-based electrolytes. Solid State Ionics 177:3199–3203